ACS Catalysis

Research Article

pubs.acs.org/acscatalysis

Dynamic Surface Processes of Nanostructured Pd_2Ga Catalysts Derived from Hydrotalcite-Like Precursors

Antje Ota,[†] Jutta Kröhnert,[†] Gisela Weinberg,[†] Igor Kasatkin,[†] Edward L. Kunkes,[†] Davide Ferri,[‡] Frank Girgsdies,[†] Neil Hamilton,[†] Marc Armbrüster,[§] Robert Schlögl,[†] and Malte Behrens*[,†,∇]

[†]Department of Inorganic Chemistry, Fritz-Haber-Institut der Max-Planck-Gesellschaft, Faradayweg 4-6, 14195 Berlin, Germany

[‡]Paul Scherrer Institut, 5232 Villigen, Switzerland

[§]Max-Planck-Institut für Chemische Physik fester Stoffe, Nöthnitzer Strasse 40, 01187 Dresden, Germany

[∇]Faculty of Chemistry, University Duisburg-Essen, Universitätsstr. 5-7, 45141 Essen, Germany

Supporting Information

ABSTRACT: The stability of the surface termination of intermetallic Pd_2Ga nanoparticles and its effect on the hydrogenation of acetylene was investigated. For this purpose, a precursor synthesis approach was applied to synthesize supported intermetallic Pd_2Ga nanoparticles. A series of Pd-substituted MgGa-hydrotalcite (HT)-like compounds with different Pd loading was prepared by coprecipitation and studied in terms of loading, phase formation, stability and catalytic performance in the selective hydrogenation of acetylene. Higher Pd loadings than 1 mol % revealed an incomplete incorporation of Pd into the HT lattice, as evidenced by XANES and TPR measurements. Upon thermal reduction in hydrogen, Pd_2Ga nanoparticles were obtained with particle sizes varying with the Pd loading, from 2 nm to 6 nm. The formation of intermetallic Pd_2Ga nanoparticles led to a change of the CO adsorption properties as was evidenced by IR spectroscopy. Dynamic changes of the surface were noticed at longer exposure times to CO and higher coverage at room temperature as a first indication of surface instability. These were ascribed to the decomposition into a Ga-depleted Pd phase and Ga_2O_3, which is a process that was suppressed at liquid nitrogen temperature. The reduction of the Pd precursor at 473 K is not sufficient to form the Pd_2Ga phase and yielded a poorly selective catalyst (26% selectivity to ethylene) in the semihydrogenation of acetylene. In accordance with the well-known selectivity-promoting effect of a second metal, the selectivity was increased to 80% after reduction at 773 K due to a change from the elemental to the intermetallic state of palladium in our catalysts. Interestingly, if air contact was avoided after reduction, the conversion slowly rose from initially 22% to 94% with time on stream. This effect is interpreted in the light of chemical response of Pd and Pd_2Ga to the chemical potential of the reactive atmosphere. Conversely to previous interpretations, we attribute the initial low active state to the clean intermetallic surface, while the increase in conversion is related to the surface decomposition of the Pd_2Ga particles.

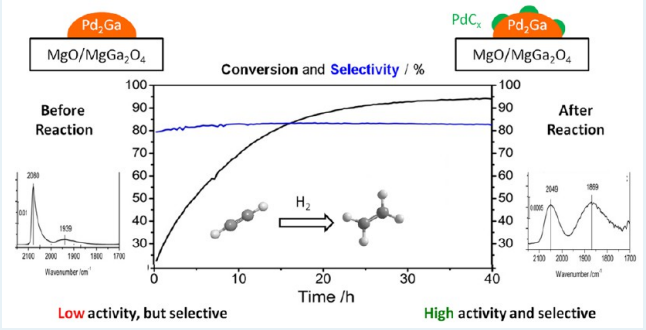

KEYWORDS: *hydrotalcite-like compounds, intermetallic compounds, palladium, CO adsorption, acetylene hydrogenation*

1. INTRODUCTION

The semihydrogenation of acetylene is of industrial relevance for polyethylene production.[1] The feed gas must be cleaned from impurities of acetylene, which otherwise poison the downstream polymerization catalyst. Thus, high selectivity toward ethylene is important to not decrease the ethylene concentration by total hydrogenation and to effectively remove traces of acetylene at the same time.

Pd-based catalysts have been known for a long time to provide an outstanding activity and selectivity for the hydrogenation of alkynes[2,3] and the reaction mechanism is discussed more detail in the Supporting Information. However, they can act in selective as well as an unselective manner and different influencing factors are discussed. Among these, the role of subsurface modifiers has recently gained high interest.[4,5] For instance, in the industrial process, eggshell Pd−Ag/Al_2O_3 alloy catalysts are applied.[6] The electronic structure of Pd can be slightly changed by alloying with Ag resulting in lower heats of adsorption for acetylene and ethylene, which favors the desorption of ethylene and thus suppresses overhydrogenation.[7−9] However, geometric effects like the reduction of the ensemble size also lead to a change in the preferred adsorption site and can disfavor the dissociative adsorption of H_2.[8] Alloys are statistically disordered and large ensembles of Pd might be still present and they are generally prone to segregate under a reactive atmosphere.[10]

Received: November 13, 2013
Published: May 13, 2014

   dx.doi.org/10.1021/cs500465r | ACS Catal. 2014, 4, 2048−2059

In this context, ordered intermetallic compounds (IMCs) have been introduced as model catalysts for a more rigid and partially covalent bonding situation in modified Pd hydrogenation catalysts. The metallurgically prepared bulk IMCs in the Pd−Ga system, Pd_2Ga[11] and PdGa[12,13] showed interesting catalytic properties. These unsupported, macrocrystalline materials were reported to show a remarkable selectivity and stability in the semihydrogenation of acetylene,[14] which were much higher compared to elemental Pd. For more-realistic catalytic application, however, these model materials should be present in the form of nanoparticles supported on a high-surface-area material.[15,16]

A feasible synthesis route of supported Pd_2Ga nanoparticles is to evenly distribute the constituent elements of the intermetallic compound and of the support in a single precursor phase. From this precursor, Pd nanoparticles are formed under reducing conditions. Upon further increase of the reduction temperature, partial reduction of the gallium species by spillover of atomic hydrogen from the metallic Pd surface[17] sets in leading to the formation of the IMC,[18] while unreduced components of the precursor constitute the oxide support. We have recently introduced a synthesis approach for Pd_2Ga intermetallic nanoparticles derived from ternary hydrotalcite (HT)-like compounds (HTlc).[11]

HTlcs allow a high flexibility of divalent and trivalent cations that are octahedrally coordinated by hydroxyl groups and build up a joint cationic lattice that is isostructural to brucite ($Mg(OH)_2$). Edge-sharing MgO_6 units form layers, which are positively charged due to the fraction of trivalent cations. Between these cationic sheets anions, together with neutral molecules, are intercalated to maintain the electroneutrality.[19] HTlcs (or layered double hydroxides, LDHs) are a widely studied class of materials due to their unique properties making them attractive for many different applications.[20−24]

In our previous work, the Pd^{2+}-, Mg^{2+}-, and Ga^{3+}-containing HTl precursor was decomposed in reducing atmospheres and yielded dispersed Pd_2Ga nanoparticles of an average size of less than 10 nm on a porous $MgO/MgGa_2O_4$ support.[11] The catalytic performance in the selective hydrogenation of acetylene was tested and compared to that of bulk Pd_2Ga.[14] We showed that apparently the catalytic properties of bulk Pd_2Ga were successfully transferred to a nanostructured and supported system. Ethylene selectivities of 70%−75% were reached at high conversion levels of acetylene in an excess of ethylene. Because of the successful nanostructuring, the metal-based activity of the ex-HTlc catalysts was higher by more than 4 orders of magnitude compared to the bulk samples. However, we also encountered a slow activation of the catalyst with time-on-stream (TOS), which is generally indicative of an in situ reconstruction of the active phase and which could not be explained so far.

In this work, a series of Pd-containing MgGa HTlc with Pd contents between 0 and 2.5 mol % was synthesized by coprecipitation. We examine the Pd^{2+} incorporation into the HTlc precursor, the role of Pd loading, the Ga reduction and the formation mechanism toward Pd_2Ga. The stability of the resulting intermetallic nanoparticles is investigated in different atmospheres and under reaction conditions. A multitechnique approach was used to characterize the precursors as well as the resulting catalysts in detail and their catalytic performance was tested in the semihydrogenation of acetylene, with special emphasis on the dynamic changes of the catalyst under working conditions.

2. EXPERIMENTAL SECTION

2.1. Synthesis Conditions. The Pd,Mg,Ga HTlc precursors were synthesized by controlled co-precipitation at pH 8.5 and 328 K by co-feeding appropriate amounts of mixed aqueous metal nitrate ($[Pd^{2+}] + [Mg^{2+}] + [Ga^{3+}] = 0.2$ M) and 0.345 M sodium carbonate solution as precipitating agent. Both solutions were added simultaneously dropwise into a 2 L precipitation reactor (Mettler−Toledo LabMax). The nitrate solution was automatically pumped with a constant dosing rate, and the basic solution was added to maintain a constant pH of 8.5.[25] After completion of the addition, the mixture was aged for 1 h at 328 K. A typical coprecipitation log is presented as Supporting Information (Figure S1). Mg^{2+} was chosen to adjust the M^{2+}/M^{3+} ratio to obtain single-phase HTlc and not to interfere with the redox chemistry of Pd and Ga. Mg, as well as residual Ga, will remain in their oxidic state and form the support material. The substitution of Mg^{2+} by Pd^{2+} in HTlc is hindered because of the larger effective ionic radius of the latter (0.86 Å, compared to 0.72 Å for Mg^{2+} (ref 26)) and its tendency toward 4-fold square-planar coordination in aqueous solutions. The precipitate was filtered and washed twice with deionized water in order to remove the NO_3^- and Na^+ ions until the conductivity of the filtrate was <0.2 mS/cm. The solid was dried for 12 h at 353 K in air. The $([Mg^{2+}] + [Pd^{2+}])/Ga^{3+}$ ratio was fixed at 70:30 and the Pd^{2+} content was varied between 0 and 2.5 mol % resulting in HTlc compositions of $(Mg_{0.7-x}Pd_x)Ga_{0.3}(OH)_2(CO_3)_{0.15}\cdot mH_2O$ with $0 \leq x \leq 0.025$. The precursors were reduced in 5 vol% H_2 in argon at 773 K to obtain the supported Pd_2Ga compounds. The heating rate was 2 K/min and the final temperature was kept for 4 h. Precursor samples will be hereafter referred to as Pd*x*, where *x* is a factor of 10 times the nominal Pd content (mol % × 10).

2.2. Characterization. For chemical analysis, ∼5 mg were exactly weighted in and dissolved in 2 mL of aqua regia. The metal content was determined by ICP-OES (Vista RL, Varian) after matrix matched calibration. The temperature-programmed reduction (TPR) experiments were performed in a fixed-bed reactor using 400 mg of precursor (100−250 μm sieve fraction). Precursors were reduced in 5 vol% H_2 in argon at a heating rate of 2 K/min (100 mL/min flow), up to a sample temperature of 773 K. The temperature was kept constant for 4 h and recorded with a thermocouple. The hydrogen consumption was monitored with a thermal conductivity detector.

Specific surface areas (SSA) of the precursors and reduced materials were determined by N_2 adsorption−desorption measurements at 77 K by employing the BET method (Autosorb-1C, Quantachrome). Prior to N_2 adsorption, the samples were outgassed at 353 K (precursors) or 423 K (reduced catalysts) to desorb moisture from the surface and pores.

X-ray absorption near edge structure (XANES) measurements at the Pd K-edge (24.350 keV) were carried out at the Super-XAS beamline at the Swiss Light Source (Villigen, Switzerland), using ionization chambers as detectors and a Si(311) Quick EXAFS monochromator. A Pd foil placed between the second and third ionization chamber was measured simultaneously as an internal reference. *In situ* XANES measurements during hydrogen TPR were performed in transmission mode, using a capillary reactor cell. The precursor (particle size 63−100 μm, 30 mg) was filled in the capillary between quartz wool plugs. The cell was connected to a gas manifold. Spectra were collected during the reduction in 5 vol % H_2/N_2 in the temperature range of 303−773 K. Reduction of the XAS data was performed using the Athena 0.8.056 software package.

For the XANES evaluation, two reference spectra for square-planar and octahedral environment were used in order to study Pd coordination geometry: a commercial PdO (puriss, Fluka) and PdZnAl HTlc (molar Pd:Zn:Al ratio = 1.0:69.5:29.5), which was prepared by coprecipitation. (With regard to the appropriateness of the latter material as a reference of Pd^{2+} in HTlc, see ref 27 and Figure S2 in the Supporting Information.) Linear combination analysis of the spectra of PdO and PdZnAl HTlc was used to obtain the fraction of Pd in MgGa HTlc present as PdO-like species in trigonal-planar and incorporated within the HTlc in octahedral coordination of oxygen.

dx.doi.org/10.1021/cs500465r | ACS Catal. 2014, 4, 2048−2059

The adsorption of CO on the reduced catalyst was studied by infrared (IR) spectroscopy. Measurements were carried out using a Perkin–Elmer Model Pe100 spectrometer equipped with a MCT detector. The spectra were recorded with a resolution of 2 cm^{-1} and an accumulation of 64 scans. Self-supported wafers were obtained by pressing the powder samples under a pressure of 123 MPa. The samples were treated directly in the IR cell, which is connected to a vacuum system with a residual pressure of $\sim 10^{-7}$ mbar. Prior the CO adsorption measurements, the samples were reduced in 500 mbar H_2 at 473 or 773 K for 2 or 4 h and then evacuated at the same temperature for 30 min. For low-temperature CO adsorption, the sample was cooled to liquid nitrogen temperature (77 K). The empty cell was used to record background spectra. Difference spectra were obtained through subtraction of the spectrum of the treated sample in vacuum from the spectrum in the presence of CO. In order to understand the activation process, which was observed during the acetylene hydrogenation (see below), the treatment was adopted comparable to the catalytic measurements. A freshly reduced catalyst was exposed to 5 vol % O_2/He for 30 min at 473 K. Afterward, pellets of this samples were pretreated at 473 K under static conditions in 200 mbar H_2 and in 10 mbar of a 1:15:30 mixture of C_2H_2:H_2:C_2H_4. The gaseous atmosphere was exchanged every 15 min to remove the evolved products. Before the CO adsorption measurements, the samples were evacuated at 473 K and subsequently cooled to room temperature.

High-resolution transmission electron microscopy (HRTEM) images were acquired using a FEI TITAN microscope, equipped with a field-emission gun (FEG) and operated at 300 kV. With computer-assisted correction and alignment, the value of the spherical aberration constant (C_s) was kept below 100 nm in the present experiments. Selected areas of the high-resolution images have been Fourier-transformed to obtain power spectra, and the lattice distances and angles were measured (accuracy of ±1% and ±0.5°, correspondingly) for phase identification. To determine the particle size distribution, projected areas have been measured and equivalent diameters of 500–2500 nanoparticles were evaluated in each sample. In all cases, the values of standard error of the mean diameter were ≤0.1 nm. Frequency distributions of the particle sizes fitted well to Gauss functions rather than log-normal functions.

2.3. Catalytic Performance in the Selective Hydrogenation of Acetylene. Measurements were performed in a quartz tube reactor at ambient pressure. A reaction temperature of 473 K was measured in the catalyst bed. The effluent of the reactor was analyzed in 20 min-intervals using an Agilent 7890A gas chromatograph equipped with a J&W Scientific Haysep Q and Agilent DB1 column, a flame ionization detector (FID), and a thermal conductivity detector. Gas-phase species up to C6 were quantified. A premixed gas mixture (Westfalen) was used, consisting of 1 vol % acetylene (2.6), 15 vol % hydrogen (5.0), 30 vol % ethylene (2.5), 5 vol % argon (5.0), and 49 vol % helium (4.6). This mixture approximates the composition of a front-end stream of a cracking process. The flow rate of the reactants was 100 mL/min. Prior to the measurements, the HTlc precursor was diluted to 100:1 with boron nitride and mixed with 1 g SiO_2 (100–250 μm), before being filled into the reactor to improve the flow characteristics. For catalytic tests, 0.2 mg of the 2.5 mol % PdMgGa HTlc was used, whereas, for the low-temperature reduction, 0.4 mg of the precursor lead to a similar conversion. The samples were reduced in situ at 473 (2 h)/773 K (4 h) in 5 vol % H_2/argon and cooled afterward to the reaction temperature. After reaching the reaction temperature, the feed gas was switched on and, after 5 min, the first chromatogram was measured. The conversion of acetylene ($X_{C_2H_2}$) and the ethylene selectivity ($Sel_{C_2H_4}$) has been calculated according to the following equations:

$$X_{C_2H_2} = \frac{r_{\text{acetylene,in}} - r_{\text{acetylene,out}}}{r_{\text{acetylene,in}}}$$

$$Sel_{C_2H_4} = \frac{r_{\text{acetylene,in}} - r_{\text{acetylene,out}}}{(r_{\text{acetylene,in}} - r_{\text{acetylene,out}}) + r_{\text{ethane}} + 2r_{C_4H_x} + 3r_{C_6H_x}}$$

It is noted that a full conversion ($X_{C_2H_2}$ = 100%) does not necessarily correspond to complete thermodynamic control, which would result in full hydrogenation of all unsaturated bonds, i.e., also of all ethylene in the feed. Internal mass transport limitations were excluded based on the Weisz–Prater criterion ($N_{W\text{-}P} = 1.7 \times 10^{-2}$).

3. RESULTS AND DISCUSSION

3.1. Structural and Textural Properties of the Precursor Material. HTlc precursors of the nominal composition $(Mg_{0.7-x}Pd_x)Ga_{0.3}(OH)_2(CO_3)\cdot mH_2O$ have been prepared by coprecipitation with Pd contents of 0–2.5 mol %. Chemical analysis shows a constant, but slightly lower than expected Mg:Ga ratio for all samples and confirms the presence of Pd in the precipitates (Table 1).

Table 1. Chemical Composition and Specific Surface Area (SSA) of the HTlc Precursors

sample	chemical composition[a] Pd:Mg:Ga (molar ratio)	SSA precursor [m^2/g]	SSA after reduction [m^2/g]	Pd content [wt %][b]
Pd0	0.0:63.2:36.8	34	130	0
Pd01	0.1:65.6:34.3	42	103	0.16
Pd03	0.3:65.8:33.9	41	113	0.56
Pd05	0.6:64.0:35.4	44	108	0.98
Pd08	0.8:65.4:33.8	44	117	1.52
Pd10	1.0:64.5:34.5	48	116	1.81
Pd15	1.6:64.5:33.9	52	106	2.79
Pd25	2.8:63.6:33.6	59	118	4.87

[a]As determined by ICP-OES. [b]Pd content after reduction at 773 K.

The XRD patterns of the HTlc precursors are shown in Figure S3 in the Supporting Information and all patterns indicate a high crystallinity and single-phase HTlc structure. No crystalline Pd-containing byproduct phase was observed up to a Pd loading of 2.5 mol %. Recently, Das et al.[28] reported about ternary PdMgAl hydrotalcite-like compounds with similarly low Pd contents and claimed incorporation of Pd^{2+} by means of XRD results. In our samples only a linear increase of the fwhm of the basal XRD peaks was observed (Table 1). The presence of Pd in the HTlc lattice probably interferes with the crystallite growth and reduces the platelet thickness significantly. These observations are in agreement with an increase in the specific surface area from 34 m^2/g to 59 m^2/g for Pd0 and Pd25, respectively (Table 1).

Scanning electron microscopy (SEM) was applied to study the morphological properties of the materials, and the results are presented in Figures S4 and S5 in the Supporting Information. Typical platelike particles were obtained for all samples and the platelets are ~1 μm in diameter and the thickness is in the order of 5–20 nm. EDX line scans revealed a homogeneous metal distribution for all three metal species within a larger aggregate of Pd01. This method detected Pd-rich areas fpr Pd15 and Pd25 suggesting that probably the upper limit for the incorporation of Pd into the HTlc layers is <1 mol %.

The analysis of the X-ray absorption near-edge structure (XANES) data, which contain information about the coordination environment of Pd, was used to determine the degree of incorporation of Pd^{2+} into the HTlc structure in our samples. Pd^{2+} prefers square planar coordination, while incorporation into the HT lattice requires octahedral coordination of the cations by oxygen ions. The low-spin d^8

dx.doi.org/10.1021/cs500465r | ACS Catal. 2014, 4, 2048–2059

electronic configuration of Pd^{2+} makes regular octahedral coordination unstable, with respect to strong tetragonal elongations. The XANES spectra of Pd10 and Pd25 precursors are shown in Figure 1. As a reference, PdO is included as a typical example for Pd^{2+} in square planar coordination of oxygen. The reference sample for the octahedral coordination of Pd^{2+} is a Pd-doped ZnAl HTlc sample, which is described in detail elsewhere[27] and shows a shape of the white line that is similar to that of Pd in distorted octahedral coordination in $LaFe_{0.95}Pd_{0.05}O_3$ perovskite.[29]

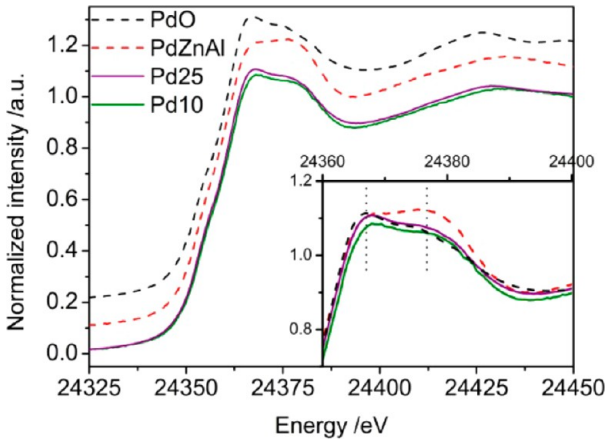

Figure 1. Normalized XANES spectra of Pd10 and Pd25 at the Pd *K*-edge. The spectra of PdO and PdZnAl HTlc are also shown and serve as reference for Pd^{2+} in square planar and octahedral coordination of oxygen, respectively.

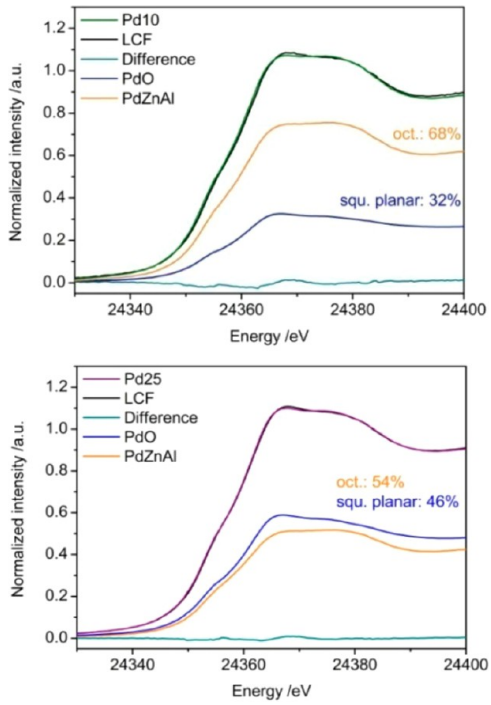

Figure 2. Linear combination fit (LCF) of Pd10 and Pd25, with respect to square planar and octahedral coordination of Pd.

While, for Pd25, 46% of Pd is incorporated into the HTlc lattice, the amount increases to 68% with decreasing Pd loading to 1.0 mol %. With respect to the total metal content, these values correspond to 1.3 mol % and 0.7 mol % Pd residing in the HT lattice in Pd25 and Pd10, respectively. Apparently, the limit for Pd incorporation into the HTlc precursors is not sharp, but seems to be ~1 mol %. Kinetic factors as well as the amount of incorporated Ga may also affect the size of the lattice site available for Pd and contribute to the amount of inserted Pd^{2+}.

In summary, a series of Pd-substituted MgGa HTl samples was successfully synthesized via coprecipitation. Pd-rich areas were noticed with increasing Pd loading, indicating a limit of incorporation of Pd into the HT lattice. XANES measurements confirmed that incorporation of Pd^{2+} in the disfavored octahedral environment is possible up to ~1 mol % of the cationic sites of the HTlc precursor.

3.2. Reduction and Intermetallic Compound Formation. The decomposition and reduction processes of the precursor samples were followed by temperature-programmed reduction (TPR) experiments. The hydrogen consumption was quantified by a TC detector and decomposition products were qualitatively analyzed by MS. In addition, in situ XANES measurements were performed to follow the formation of Pd_2Ga.

Upon feeding of hydrogen over the precursors at room temperature, it was rapidly consumed. Depending on the Pd content, between 10 and 100 min were necessary to stabilize the TCD signal and subsequently the samples were heated to 773 K in the hydrogen flow. For Pd10 and Pd25, the experimental hydrogen consumptions are 7.2 μmol and 61.7 μmol, respectively, and correspond to reduction of 25% and 54% of the total Pd content at room temperature. These values are in reasonable agreement with the fraction of segregated PdO-like Pd species of 32% and 68% not incorporated in the HT lattice, as estimated by XANES. The segregated species is assumed to be reduced at lower temperature compared to Pd^{2+} in the HT lattice. Interestingly, up to a Pd content of 0.8 mol %, only minor amounts of hydrogen were consumed at room temperature. This indicates that the vast majority of Pd^{2+} is octahedrally coordinated and stabilized in the HT lattice against room-temperature reduction (RTR). Using the TPR experiments as an indicator, full incorporation of Pd in the HT lattice is detected for the sample Pd01 as no RTR signal was obtained.

Figure 3 illustrates the TPR profiles after completion of RTR for various Pd loadings. In general, two signals were observed for the Pd-doped samples during heating. A low-temperature reduction (LTR) peak occurs at between 383 K and 403 K. This peak is assigned to the reduction of Pd^{2+} incorporated into the HT lattice to metallic Pd. With increasing Pd loading, a slight shift to lower temperatures is observed, probably due to the increasing Pd concentration in the precursor that facilitates formation of metallic particles.

The degree of Pd reduction was calculated from the H_2/Pd ratio and is given as a percentage, where 100% corresponds to the stoichiometric reduction of PdO ($PdO + H_2 \rightarrow Pd + H_2O$). It was found to decrease with increasing Pd content (Table 2). There is a hydrogen excess of 216% for Pd01, while it is

dx.doi.org/10.1021/cs500465r | ACS Catal. 2014, 4, 2048−2059

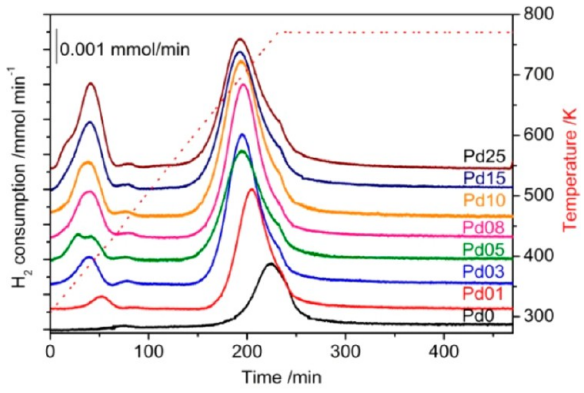

Figure 3. Temperature-programmed reduction (TPR) profiles of the HTlc precursors in 5% H_2/argon.

Table 2. Quantification of the TPR Experiments

sample	Pd[a] [wt %]	Ga[a] [wt %]	T_{LTR}[b] [K]	T_{HTR}[c] [K]	Pd RTR[d] [%]	Pd LTR[e] [%]	sum, RTR + LTR[f] [%]
support	0	25.8		732			
Pd01	0.10	25.2	403	709	0	216	216
Pd03	0.35	25.1	395	700	10	140	150
Pd05	0.61	25.8	387	696	5	129	134
Pd08	0.94	24.9	384	697	15	107	121
Pd10	1.13	25.2	382	694	26	102	128
Pd15	1.73	24.7	387	693	70	85	155
Pd25	3.01	24.2	386	692	61	70	131

[a]Pd and Ga content of the precursor determined by ICP-OES. [b]Low-temperature reduction (LTR). [c]High-temperature reduction (HTR). [d]Theoretical degree of Pd reduction at room temperature (RTR). [e]Theoretical degree of Pd reduction at low temperature (LTR). [f]Total hydrogen consumption at RT and LTR related to the Pd content of the samples.

significantly decreased to 70% for Pd25. Taking the amount of hydrogen consumed in RTR also into account, the value of H_2/Pd always exceeded 100%. This excess is probably attributed to PdH_x formation and spillover hydrogen from the metal to the support. Iwasa et al.[30] reported on TPR studies of Pt and Pd nanoparticles supported on several oxides (for instance, ZnO, Ga_2O_3, MgO, and Al_2O_3). They also observed higher hydrogen consumptions at room temperature than required to reduce the Pd^{2+} present in their samples. Formation of a PdH_x phase was concluded and confirmed by *in situ* XRD. In addition, desorption of hydrogen from PdH_x produced weak inverse peaks at ~323−363 K. In contrast to the work of Iwasa et al.,[30] no desorption was observed for our samples, which might be a result of different particle sizes.[1]

A high-temperature reduction (HTR) peak is observed between 693 K and 709 K for all HTlc samples. The HTR peak is significantly shifted to lower temperature with increasing Pd content. The peak maxima shifts from 732 K (Pd0) to 692 K (Pd25). The amount of hydrogen does not fit to Ga oxide reduction related to stoichiometric formation of Pd_2Ga, but indicate too high of a Ga^0 formation (between 5% and 25% of the total Ga content during HTR in Pd0 and Pd25, respectively). These large values can be explained by the additional hydrogen consumption due to the reverse water-gas shift reaction that occurs in the same temperature range with CO_2 from carbonate decomposition. Product CO has been observed with mass spectrometry as discussed in the Supporting Information in detail (Figure S6). Hence, the hydrogen consumption of the HTR peak has at least two contributions. It is related CO formation and to Ga oxide reduction and intermetallic compound formation.

XANES was applied to better resolve the changes happening during HTR. Figure 4 shows the *in situ* XANES spectra of the

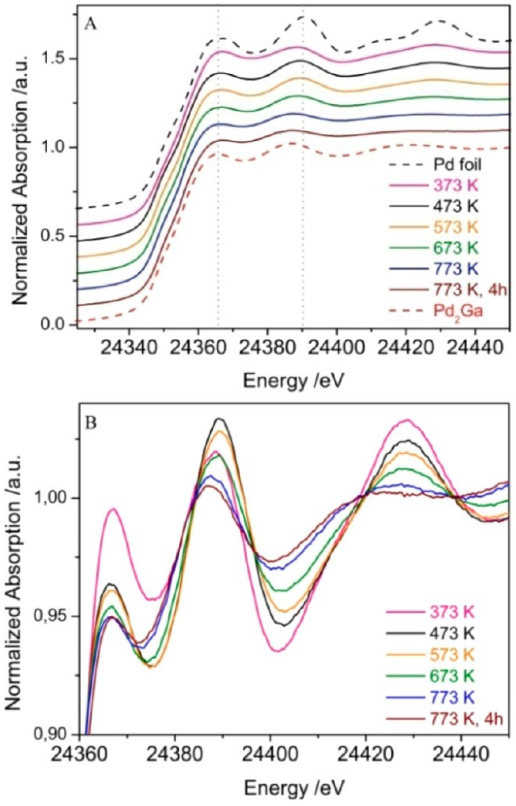

Figure 4. Normalized XANES spectra of Pd25 during reduction. Pd foil and bulk Pd_2Ga are added as references (black and red dashed lines).

Pd25 precursor collected during reduction in hydrogen, compared with palladium foil and bulk Pd_2Ga (dashed black and red line, respectively). The most notable differences between the two references are generally lower amplitudes of the oscillations and a slight shift of the spectral features at 24 390 and 24 429 eV of bulk Pd to lower energies (24 387 and 24 420 eV) for bulk Pd_2Ga. A detailed representation of Pd25 is shown in Figure 4B. With increasing reduction temperature and time the damping as well as the low-energy shift of the spectral features can be observed. With the exception of the spectrum collected at 373 K (pink line), which according to TPR and in agreement with the strong white line still contains oxidized Pd, five isosbestic points of the spectra are observed, suggesting that Pd-containing intermediates such as the face-centered cubic (fcc) Ga−Pd alloy or IMCs cannot be detected in this experiment resembling a direct transformation of Pd metal into Pd_2Ga. The XANES experiments confirm that the formation of intermetallic Pd_2Ga from metallic palladium is completed when the temperature is kept constant at 773 K.

Summarizing this part, upon thermal reduction in hydrogen the precursor is decomposed and is transformed to supported intermetallic Pd_2Ga nanoparticles. TPR and XANES measurements confirm that a temperature of 773 K is needed for complete transformation of Pd to Pd_2Ga nanoparticles.

dx.doi.org/10.1021/cs500465r | ACS Catal. 2014, 4, 2048−2059

3.3. Structural Properties of Pd_2Ga Nanoparticles.

TEM analysis was used to study the morphology and phase of the Pd-containing particles as well the support. Selected samples with different Pd loadings were investigated, with respect to particle size and phase composition. Furthermore, the influence of reduction temperature and the exposure to air after reduction were studied.

As seen in Figure 5, the reduction of Pd10 at 773 K yields metallic particles that appear as dark spots and are supported by

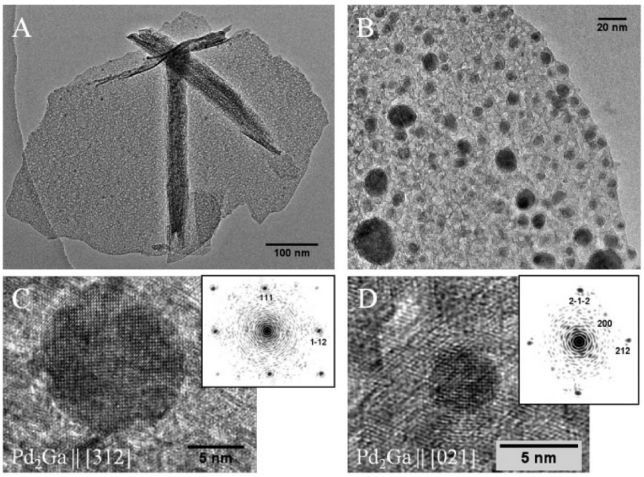

Figure 5. (A, B) Overview micrographs and (C, D) HRTEM images of Pd10 with corresponding FFT pattern after reduction at 773 K.

an oxide matrix. The platelet-like morphology is maintained upon decomposition and reduction (Figure 5A). XRD and HRTEM analysis reveal that the oxide support consists of MgO and $MgGa_2O_4$ spinel (see Figure S7 in the Supporting Information). In some HRTEM images (Figures 5C and 5D), the metallic phase is unambiguously identified as Pd_2Ga. In certain orientations and for lower Pd loadings, however, the phase identification is ambiguous, because of small, highly defective particles and similar lattice fringes of Pd_2Ga and Pd, which are structurally related[31] (see Figure S8 in the Supporting Information).

The determined average metal particle sizes of Pd05, Pd10, and Pd25 after HTR are 1.8, 6.1, and 4.8 nm, respectively. Monomodal particle size distributions are obtained with narrow particle sizes, as presented in Figure 6.

Furthermore, the surface of the nanoparticles is often covered by a partially disordered layer. To exclude that oxidation of Pd_2Ga in air was the origin of the oxide shells, Pd25 was investigated without air exposure. Nevertheless, a uniform overlayer around the intermetallic particles are observed as shown in Figure 7. Based on the lattice fringes, these shells are identified either as cubic Ga_2O_3 (γ-phase), $MgGa_2O_4$, or other Pd_xGa_y phases, while Pd, PdO, and MgO can be excluded. Because of the strong contrast of the shell to the metallic particle core, the oxides seem more likely than Pd_xGa_y phases.

Surface coverage of noble metals is often associated with reducible supports and is widely discussed in terms of strong-metal support interaction (SMSI). SMSI influences the chemisorption properties of the metal depending on the reduction temperature.[32,33] Full access to metal surface is only possible at low reduction temperature while, at high temperature, the chemisorption capability is heavily disturbed by oxide

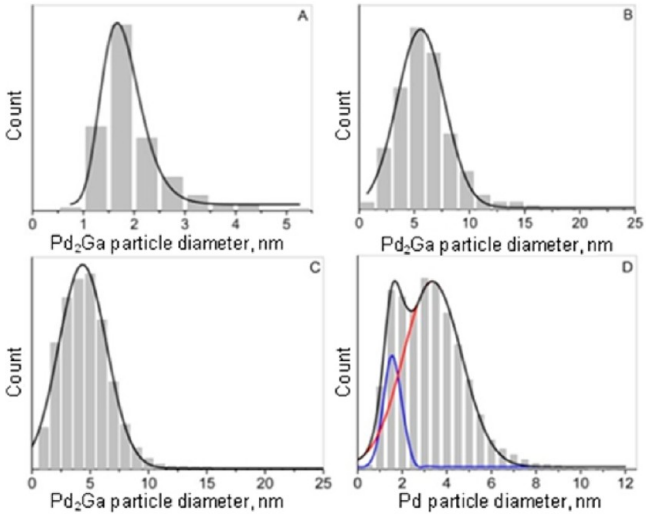

Figure 6. Particle size distribution of (A) Pd05, (B) Pd10, and (C) Pd25 after HTR (773 K), and (D) Pd25 after LTR (473 K).

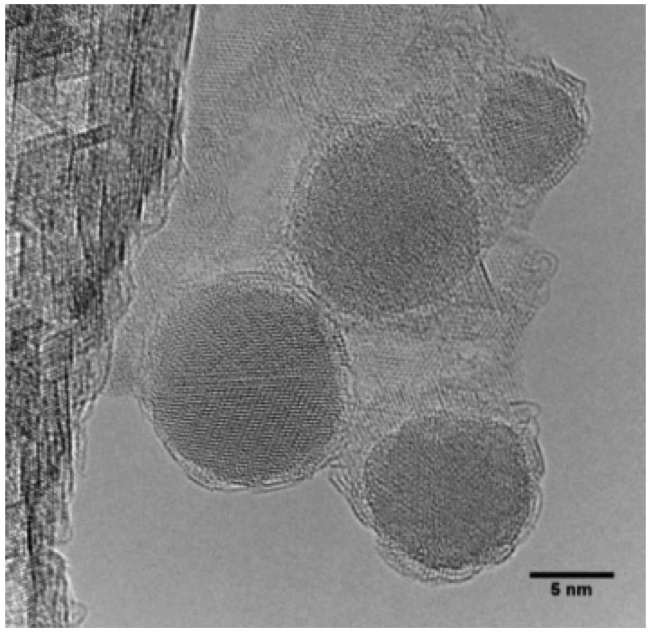

Figure 7. HRTEM images of Pd25 after reduction without air contact.

encapsulation of particles.[34] This phenomenon is reversible, i.e., reoxidation and mild reduction allows the catalyst to recover the original chemisorption capacity. The morphology of Pd25 was also studied after LTR at 473 K (Figure 8). According to the XANES spectrum, Pd_2Ga has not yet been formed at this temperature. Careful investigation of the electron diffraction pattern confirms that the main crystallographic phase is metallic Pd, as shown in Figure 8C. The Pd particles show a bimodal size distribution (Figure 6D). A minor fraction exhibits an average size of 1.6 nm, whereas, for the larger fraction, the particle size is 3.3 nm. We suggest that the smaller particles originate from Pd^{2+}, which was incorporated into the HTlc layers and the larger ones from segregated PdO-like Pd^{2+}. Upon temperature increase to 773 K, the particles have grown at the expense of the smaller ones and result in an average particle size of 4.8 nm (Figure 8C). Interestingly, particle encapsulation and core−shell structures were also observed upon reduction at 473 K, as illustrated in Figure 8B. The encircled areas in Figure 8A

dx.doi.org/10.1021/cs500465r | ACS Catal. 2014, 4, 2048−2059

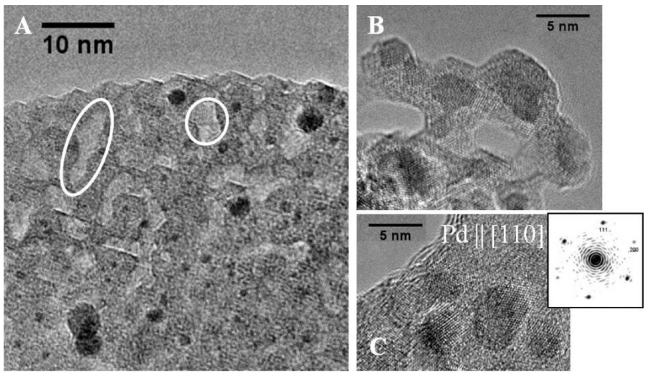

Figure 8. (A) Overview micrograph and (B, C) HRTEM photomicrographs of Pd25 after LTR (473 K) and the corresponding FFT pattern.

are identified as crystalline $MgGa_2O_4$ spinel that is formed in addition to amorphous spinel phase and MgO upon reduction.

An alternative (or additional) origin of the surface-covering layer is the oxidative decomposition of the Pd_2Ga nanoparticles. It was recently shown by Leary et al.[35] that the surface termination of Pd_2Ga nanoparticles can differ considerably from the bulk and disordered overlayers have been observed, probably as a result of oxidative surface decomposition. Our samples have been transferred to the TEM, avoiding air contact, but it has been shown recently by Wowsnick et al.[36] by in situ XPS that traces of oxygen already are sufficient to trigger decomposition of Pd_2Ga at the surface. We thus cannot exclude that oxidative impurities in the glovebox or TEM sample holder are responsible for the effect seen in Figure 7.

In summary, TEM analysis was applied to determine the Pd-containing phase and give estimation of the particle size. A reduction temperature of 473 K leads to bimodal distribution of metallic Pd, which is explained by the partial incorporation of Pd^{2+} in the HTlc precursor. Larger particles but with monomodal size distribution are obtained for samples reduced at 773 K. The particle size of Pd_2Ga can be controlled by Pd loading, to a certain extent, and varies between 2 nm and 6 nm. Furthermore, the appearance of surface covering is noticed, indicating a possible SMSI state of the catalysts and/or surface decomposition.

3.4. IR Characterization of Supported Pd_2Ga Nanoparticles during Exposure to CO. The adsorption properties of the Pd phases obtained after LTR and HTR, as well as the interaction of CO with the oxide support, were investigated by IR spectroscopy. The spectra displayed in Figure 9 exhibit characteristic bands in the carbonyl region of 2100−2000 cm^{-1} and 1970−1800 cm^{-1}. These bands are typical for linearly and multiply bonded CO on metallic Pd surfaces, respectively.[37,38]

As already mentioned, reduction of the PdMgGa HTlc precursors at only 473 K resulted in metallic Pd particles. CO adsorption of this sample at RT and a pressure of 50 mbar lead to population of on-top (2074 cm^{-1}), 2-fold bridging (1983 cm^{-1}), and 3-fold hollow sites (1896 cm^{-1}) on Pd^0 (Figure 9A). A coverage-dependent shift was observed for all bands ($\Delta\upsilon$ = +25 cm^{-1}), because of increased dipole−dipole coupling. In addition, a sharp band at 2016 cm^{-1} emerged during CO exposure at elevated pressures above 1 mbar. According to the literature, it is either related to carbidic areas of the Pd sites due to CO disproportionation[39] or attributed to isolated Pd sites, whose electronic properties are modified by interaction with basic support species.[40]

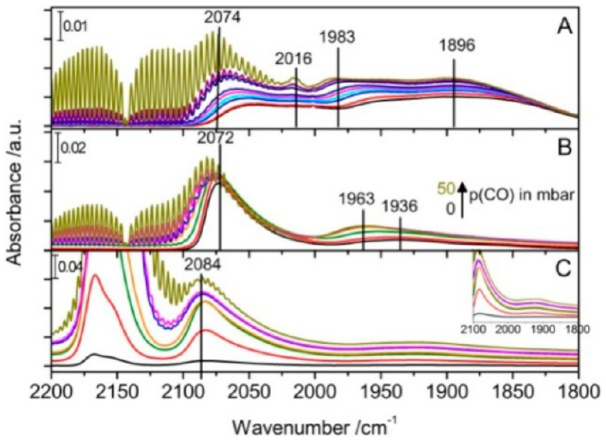

Figure 9. IR spectra of CO adsorbed on Pd10 (A) after LTR (473 K) and (B) after HTR (773 K) recorded at RT, and (C) after HTR recorded at 77 K in the CO stretching region from 2200−1800 cm^{-1}. (IR bands above 2100 cm^{-1} are due to physisorbed CO.) It is noted that CO pressures above 1 mbar give rise to gas-phase rotational bands of CO.

HTR at 773 K modifies the ratio of multiply bonded to linearly adsorbed CO on Pd−Ga surfaces, as shown in Figures 9B and 9C, and as reported in the literature.[41] The spectra indicate an isolation of the adsorption sites by Pd_2Ga formation. At RT adsorption (Figure 9B) and low CO pressure, predominantly on-top coordinated CO (2072 cm^{-1}) is present with only a weak band due to multiply bonded CO at 1936 cm^{-1}. With increasing pressure, the latter band grows and shifts to 1963 cm^{-1}. In contrast, CO adsorption at 77 K prevails one predominant band at 2084 cm^{-1} and no change of the band due to multiply bonded CO, even at increased CO pressures, was observed (see Figure 9C and the inset). This observation indicates a change of the catalyst's surface in the presence of CO, which was described in detail by Föttinger.[41]

While at low temperature, CO is mostly unreactive and only small amounts of monodentate and bicarbonate species were formed in the carbonate region (1700−1200 cm^{-1}), pronounced formation is observed at room temperature (Figure 10). The signals located at 1650, 1546, and 1340 are ascribed to $\upsilon_{as}(CO_3^{2-})$ and $\upsilon_{sy}(CO_3^{2-})$ modes of monodentate and bidentate carbonate species. The more-intense bands,

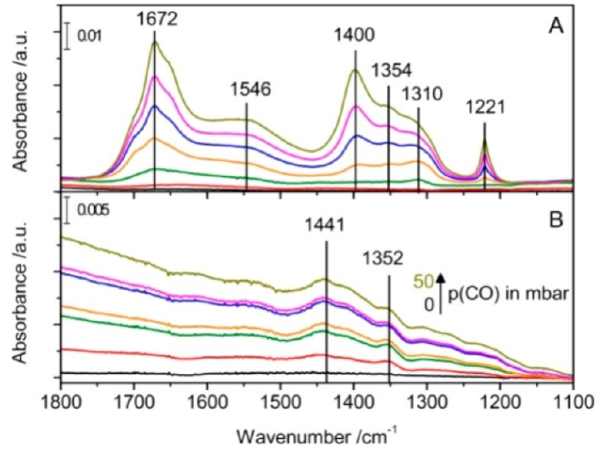

Figure 10. IR spectra of CO adsorbed on Pd10 after HTR in the carbonate region from 1800−1100 cm^{-1} at (A) RT and (B) 77 K.

dx.doi.org/10.1021/cs500465r | ACS Catal. 2014, 4, 2048−2059

located at 1671, 1400, and 1221 cm^{-1}, are assigned to $\upsilon_{as}(CO_3^{2-})$, $\upsilon_{sy}(CO_3^{2-})$, and $\delta(OH)$ modes, respectively, of surface bicarbonate species (HCO_3^-).[42,43] The formation of different carbonate species can be either related to CO dissociation/disproportionation ($2CO \rightarrow CO_2 + C$)[39,43] or direct reaction of CO with hydroxyl groups on the surface to CO_2 ($CO + OH \rightarrow CO_2 + {}^1/_2H_2$).[44] The CO_2 formed further reacts with O^{2-} or OH groups of the support to form carbonate and bicarbonate. For our samples, the observed changes in the OH stretching suggest the reaction of CO with hydroxyl groups instead of CO disproportionation. The released hydrogen can further react with surface OH groups to give water (${}^1/_2H_2 + OH \rightarrow H_2O$). Water evolution (3346 cm^{-1}) and bicarbonate formation (3621 cm^{-1}) occurred simultaneously in our experiment (see Figure S9 in the Supporting Information).

The absence of the bridge-bonded band at 77 K suggests that carbonate (and water) formation and the population of an additional multiply bonded adsorption site are correlated with each other. The slow population of these sites at wavenumbers below 2000 cm^{-1} can be interpreted as the beginning formation of extended Pd−Pd contacts at the surface, because of the decomposition of the intermetallic surface as present in elemental Pd. This behavior corresponds to a reversal of the isolation of the Pd sites that has been observed as a result of IMC formation. We observed such evolution toward metallic Pd also for samples after air exposure or pretreatment at insufficient high reduction temperature (not shown). Furthermore, unsupported bulk Pd_2Ga samples have been shown to decompose upon milling in air into elemental-like Pd and Ga_2O_3 at the surface.[36]

For our samples, an increase in reduction temperatures and longer reduction periods has shown to minimize the contribution of bridged-bonded carbonyl band and reform the intermetallic surface (not shown). We thus conclude that CO at sufficient temperature and pressure reacts with the surface of our $Pd_2Ga/MgO/MgGa_2O_4$ materials. This dynamic response of the surface to CO leads to partial decomposition of the intermetallic surface and formation of neighboring elemental-like Pd surface species, as indicated by the appearance of multiply bonded CO adsorbates. Initially, isolated adsorption sites on the Pd_2Ga surface responds to CO exposure in a way that suggests an (at least partial) breakup of the intermetallic compound into surface regions containing Ga-depleted metallic Pd species. Our observations are in agreement with results reported by Haghofer et al.,[45] who concluded formation of elemental Pd patches on the surface of Pd_2Ga particles. Although carbon monoxide itself is a reducing gas, it clearly induces modifications of the intermetallic compound and the support at relevant temperatures. Hence, we assume that dynamic changes of the oxide support (carbonate and water formation), in combination with the high oxophilicity of gallium, give rise to the partial decomposition of Pd_2Ga nanoparticles into finely dispersed Pd and oxidized Ga. The consequences for the interpretation of the volumetric CO chemisorption data and additional IR results are discussed in the Supporting Information (see Figures S10 and S11).

In summary, CO-IR adsorption measurements highlight the presence of isolated adsorption sites by formation of intermetallic Pd_2Ga nanoparticles. While, at 77 K, only one distinctive carbonyl band at 2080 cm^{-1} is formed and no spectral changes were observed with increasing CO coverage, the Pd_2Ga surface is apparently instable upon inserting CO in the chamber at RT. It suggests that, in contrast to the bulk model catalysts, Pd_2Ga nanoparticles are highly reactive toward different gas atmosphere, because of an increased number of surface atoms as a result of the nanostructuring. CO exposure of the surface leads to the partial oxidation of metallic Ga, probably by oxidizing species (CO_2 and H_2O) originating from the interaction of CO with the support material, and the formation Ga-depleted Pd on the surface of the particles.

3.5. Catalytic Performance. In this part, the catalytic experiments, which were performed in order to better understand the previously observed activation behavior[11,46] at a reaction temperature of 473 K, will be presented and related to the structural properties addressed in the previous sections of this work. Prior to the catalytic measurements, the HTlc precursor was reduced in the reactor in 5% H_2/argon at low reduction temperature (473 K) and high reduction temperature (773 K).

Figure 11 shows the acetylene conversion and ethylene selectivities for all experiments over TOS. A different catalytic

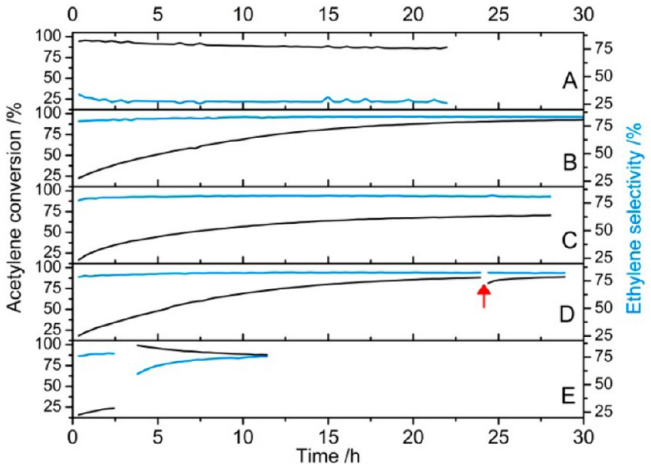

Figure 11. Acetylene conversion and ethylene selectivity at 473 K over (A) Pd25 reduced at 473 K, (B) Pd25 reduced at 773 K, (C) Pd25 reduced at 773 K and treated in 5 vol% H_2/argon at 473 K, (D) Pd25 reduced at 773 K with O_2 pulse after 24 h TOS (arrow), and (E) Pd25 reduced at 773 K and treated in O_2 after 2.5 h TOS at 473 K for 40 min.

performance was obtained, depending on the reduction temperature. LTR yields a catalyst that slowly deactivates with TOS (Figure 11A), probably because of the formation of carbonaceous deposits.[1] The selectivity toward the desired semihydrogenation product is relatively stable at only 26% after 22 h TOS. As it was shown in the previous sections, a reduction temperature of 473 K is not sufficient to form the intermetallic compound. Accordingly, the catalytic properties—low selectivity and low stability—are representative of pure Pd rather than that of the intermetallic compound Pd_2Ga.

If a reduction temperature of 773 K was applied (HTR), which has been shown above to be sufficient to create Pd_2Ga nanoparticles, a remarkable change in the catalytic properties is observed (see Figure 11B). As reported previously,[11] a slow and pronounced activation from 22% to 94% conversion is seen within the first 30 h TOS. After 44 h TOS, the ethylene selectivity has increased to 80%, while the selectivities to C_2H_6, C_4, and C_6 hydrocarbons are each below 10%, as shown in Figure S12 in the Supposing Information. Interestingly, only slight changes in the selectivity are observed during the

dx.doi.org/10.1021/cs500465r | ACS Catal. 2014, 4, 2048−2059

pronounced activation. After stabilization, this highly active and selective state of the catalyst is characterized by an apparent activation energy of 37 kJ/mol, which is on the lower end of what was reported previously for acetylene hydrogenation over Pd catalyst (Figure S13 in the Supporting Information).[47]

Two different possible explanations will be discussed in the following. Corresponding models of the active state of the nanostructured Pd_2Ga catalyst are schematically shown in Figure 12. Model I is only related to an increased accessibility

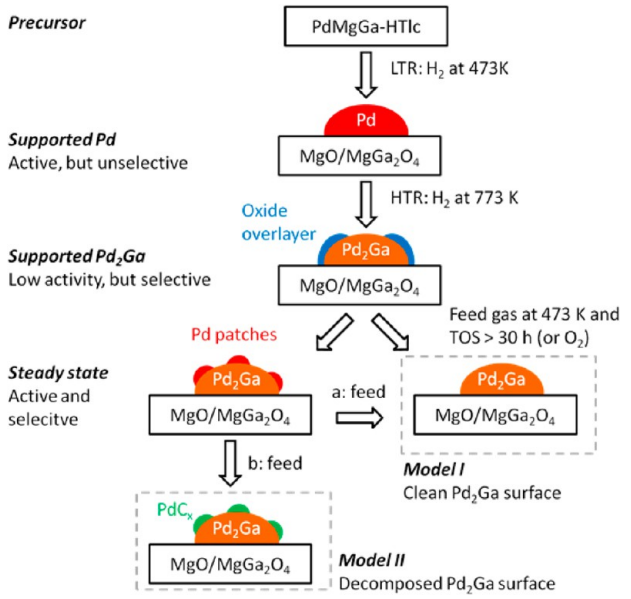

Figure 12. Schematic models explaining the activation process during the selective hydrogenation of acetylene.

of the intermetallic surface, while Model II includes changes in the nature of the active sites as well as modifications by the feed gas. The fundamental difference of both models is that, according to Model I, the intermetallic surface is the catalytically active state, while in Model II the decomposition product of the intermetallic compound is active.

Model I refers to the SMSI state of the catalyst that causes partial blocking of the active surface and was detected by TEM after HTR. The removal of the oxide shell formed at HTR can be triggered by reoxidation and mild reduction,[32] but also a lower reduction potential by decreasing the temperature from 773 K (reduction) to 473 K (reaction) might be sufficient to slowly reverse the SMSI state and is a possible explanation of the observed activation. The catalyst after HTR was further pretreated in 5% H_2/Ar for 16 h at reaction temperature (473 K) to check if the activation occurs with time also under milder reducing conditions in the absence of the reactant feed. The corresponding reaction profile of the pretreated sample is shown in Figure 11C. No substantial differences of the activation process are observed in comparison to profile B. The activation time is comparable to that of the catalyst without any further pretreatment after reduction. Thus, either the SMSI state has not been reversed because of the difference in the redox potentials of the 5% H_2/Ar stream and the 1% C_2H_2/15% H_2/30% C_2H_4 reaction mixture at 473 K or the activation process is caused by another modification of the Pd_2Ga surface in the feed gas.

According to the IR results, the decomposition of the intermetallic compound into Ga-depleted Pd species and oxidized Ga species can be responsible for the slow activation behavior of the catalyst. This segregation is represented in Model II. Under reaction conditions, the required oxygen may come from O-containing impurities in the feed gas or from the support, similar as discussed for CO adsorption at room temperature. The increase in activity can be explained by the formation of highly reactive, metallic Pd patches on the particle surface as reported for larger Pd_2Ga particles during methanol steam reforming.[45] Model II relies on the assumption that the ethylene selectivity of the less active initial Pd_2Ga surface measured at low conversion and that of the more active, metallic Pd particles at higher conversion must be coincidently similar, so that a clear effect in conversion but only a minor effect in selectivity is observed during activation. The metallic Pd patches resulting from decomposition are expected to be very small, much smaller than the Pd_2Ga particles. Therefore, hydride formation, which is known to be size-dependent[1] and was shown to be responsible for the unselective hydrogenation of alkynes,[48,49] will most probably not occur. Thus, the newly formed Pd^0 patches might be highly selective, because of their small size.

The transformation of the Pd patches into a PdC_x phase in the feed is also a possible explanation for the high selectivity of the decomposed surface.[50] Small palladium particles have a larger tendency to form the PdC_x phase[51] by the fragmentation of the reactant molecules, which also hinders subsurface hydride formation. Neither hydride nor carbon formation were observed for bulk intermetallic compounds,[52,53] but seems to play a role for the nanostructured Pd_2Ga compound, which is more reactive due to the increased number of surface atoms or tend to decompose, as suggested by Model II.

To investigate the activated state of the catalyst, 50 mg of undiluted Pd25 precursor were reduced *in situ* and activated in 150 mL/min feed gas flow for 44 h TOS. TEM analysis of this sample was done without air contact in order to keep the metallic state of the particles. Micrographs with different magnifications are presented in Figure 13.

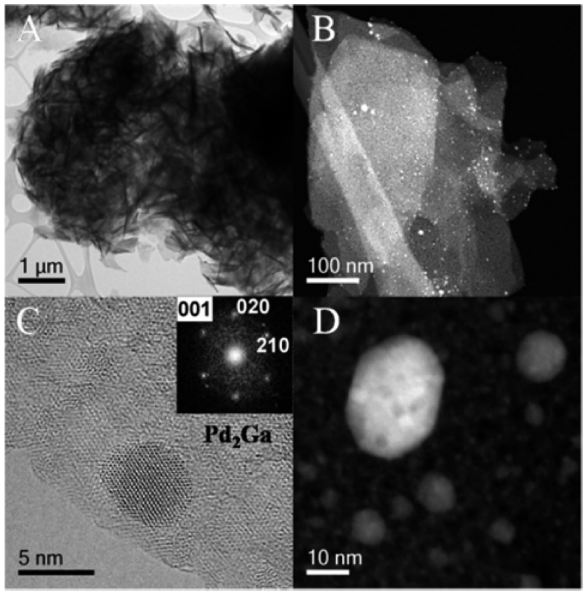

Figure 13. (A) TEM overview micrograph; (B, D) STEM images; (C) HRTEM micrographs (with FFT pattern of Pd_2Ga along (110) zone axis) of post-reacted Pd25 catalyst after 44 h TOS.

dx.doi.org/10.1021/cs500465r | ACS Catal. 2014, 4, 2048−2059

Phase identification on the basis of the lattice fringes seen in the bright-field images suggests that the intermetallic compound Pd_2Ga is preserved in the core of the nanoparticles during activation (Figure 13C). However, the particles exhibit contrast fluctuations in the scanning TEM images, indicative of an inner inhomogeneity (Figure 13D). Different types of material which differ in their Z-contrast seem to have segregated, supporting the partial surface decomposition of the Pd_2Ga IMC into a metallic and an oxidic species during activation, as suggested by Model II. Unfortunately, it was not possible to identify the involved phases that are the origin of the contrast fluctuations. No indication for formation of amorphous carbon deposits is found. The absence is also confirmed by Raman spectroscopy, which shows no characteristic bands for amorphous carbon (see Figure S14 in the Supporting Information). However, a temperature-programmed oxidation by TG-DSC-MS showed an exothermic mass loss of 3% that was associated with CO_2 formation is observed up to a temperature of 773 K (Figure S15 in the Supporting Information). This corresponds to an amount of 6 μmol of carbon. Considering that changes in the catalytic properties of Pd catalysts by carbonaceous deposits are typically reported to promote the selectivity rather than the activity in hydrogenation reactions,[54] they are not considered here as a reason for the catalyst activation, but might indicate in situ formation of PdC_x and thus have an effect on the selectivity.

Since the Pd_2Ga surface is known to be oxygen-sensitive,[36,45] the role of oxygen addition was studied (see Figures 11D and 11E). In the first experiment, the catalyst was exposed to three pulses of O_2 (each 10 μmol) after activation in feed for 24 h at 473 K (Figure 11D, indicated by the red arrow). The unperturbed catalytic performance suggests that either the intermetallic surface has already been completely decomposed during the activation and cannot react any further with gas phase oxygen (Model II), or that the reducing potential of the feed gas at 473 K is sufficient to instantaneously clean the surface again and reform the oxygen-free state of the intermetallic surface (Model I). The catalyst was also exposed to three O_2 pulses directly after reduction and before switching to the reaction feed at 473 K. No significant impact on the catalytic performance was observed at the beginning of the activation period (see Figures 11D and 11E), which confirms a certain stability of the surface against low amounts of dry oxygen and indicates that H_2O, as identified in the IR experiments, might have a stronger decomposing effect on the intermetallic than O_2.

After 2.5 h TOS, the catalyst was treated in a 5% O_2/He flow for 40 min at 473 K. This treatment is estimated to be harsh enough to trigger an oxidative surface decomposition of the intermetallic surface. As illustrated in Figure 11E, this treatment transforms the catalyst directly to a more active state. However, compared to the state obtained after prolonged TOS, the selectivity is initially considerably lowered. This is likely a result of the presence of highly active metallic Pd, which has formed from the IMC decomposition. Because of the lower intrinsic selectivity of monometallic Pd (cf. Figure 11A) and/or as a consequence of transiently reached 100% conversion, the selectivity is decreased. It fully recovers to the expected value of 80% within the following 7.5 h TOS, while the conversion drops again to a similar level, as observed in the other experiments. This result shows that the dynamics triggered by the O_2 treatment is faster than the activation in the feed, but finally leads to the same surface state with the same catalytic performance. It is noted that catalysts that have been removed from the reactor after HTR and stored in air did not show the slow activation behavior, but directly this more active state, indicating that air contact has a similar decomposing effect, like the O_2 treatment.

The effect of O_2 treatment can be explained by both models—the oxidative reversal of the SMSI state with subsequent self-cleaning of the intermetallic surface in the feed (Model I), as well as the accelerated oxidative decomposition—which leads to the formation of a different active state, which can undergo further transformation in the feed (Model II). In the latter case, two pathways are possible for such transformation under reaction conditions, as shown in Model II (panels (a) and (b) in Figure 12). Either the evolving metallic Pd patches on the Pd_2Ga particles are unique and selective (e.g., because of their small particle size (Figure 12a) or the dispersed Pd patches undergo a slow transformation to a highly selective PdC_x phase (Figure 12b).

By means of CO-IR spectroscopy, a catalyst which was treated in oxygen for 30 min at 473 K was studied. Figure 14A shows the IR spectra of adsorbed CO of the fresh Pd_2Ga catalyst directly after HTR with primarily on-top coordinated CO indicative of the IMC surface. After O_2 treatment and a subsequent mild reduction in H_2 (Figure 14B) and in feed gas (Figure 14C) at 473 K characteristic bands of linearly and multiply bonded CO are present. This increased contribution of multiply bonded CO supports the decomposition of Pd_2Ga upon O_2 treatment and is indicative of a Pd-like surface state. From the comparison of Figures 14A and 14C, which displays the true active state of the catalyst, the reformation of the intermetallic surface state in the feed can be excluded. Furthermore, compared to the spectrum obtained after H_2 reduction, which is typical of monometallic Pd, the spectrum of the sample that was activated 7 h in the feed gas is shifted to

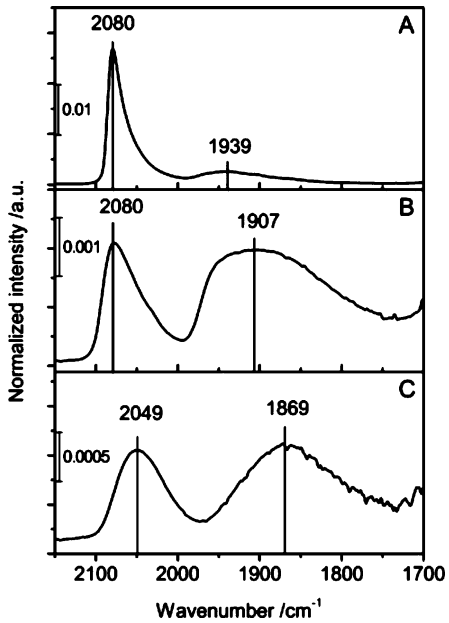

Figure 14. CO-IR adsorption spectra of (A) Pd25 after HTR for 4 h; (B) after subsequent treatment in O_2 (5 vol %, 30 min, 473 K) and H_2 (200 mbar, 2 h, 473 K); (C) after subsequent treatment in O_2 (5 vol %, 30 min, 473 K) and $H_2/C_2H_2/C_2H_4$ mixture (10 mbar, 7 h, 473 K). (The shown spectra were recorded at a CO pressure of 0.08 mbar.)

dx.doi.org/10.1021/cs500465r | ACS Catal. 2014, 4, 2048−2059

lower wavenumbers ($\Delta\upsilon = -31$ cm^{-1}) and the band shape has changed. This suggests that the Pd patches formed by the decomposition process undergo a further transformation in the feed and favors Model IIb, i.e., the formation of a highly selective PdC_x phase. The exposure to reaction feed, which is sufficient to reach the active state in the catalytic measurements, is not sufficient to the reform the intermetallic state, as shown in Figure 14C, indicating that the active phase is indeed not the clean intermetallic Pd_2Ga surface.

This interpretation is in good agreement with liquid-phase hydrogenation data reported by Wowsnick et al.,[46] who showed that the clean intermetallic surface of unsupported Pd_2Ga was considerably less active in compared to a decomposed surface without a pronounced effect on selectivity. This study also confirmed the strong instability and easy passivation of the intermetallic surface state against even traces of oxidizing impurities, which is in agreement with the observations reported here, i.e., an ongoing oxidative decomposition in CO or hydrogenation feed mixtures despite the virtual absence of oxygen or water.

In summary, the supported nano-Pd_2Ga catalyst obtained after high-temperature reduction at 773 K show slow activation in the feed gas. Alternatively, activation in oxidative atmosphere can enhance the reactivity faster. In both cases, a highly selective catalyst can be obtained. Not considering carbon deposits as the reason for this behavior, the results are consistent with two possible explanations for the activation. The first is the removal of surface coverage formed due to the SMSI effect at high reduction temperature. Second, similar to the dynamic processes occurring in CO atmosphere, the instability of the Pd_2Ga surface, induced by the reaction atmosphere (C_2H_2, C_2H_4, dissociated H or O_2), lead the partial decomposition to metallic Pd and formation of new very active and selective sites for hydrogenation. While we cannot unambiguously exclude the one or the other model, the data presented and recent results reported in the literature on this catalyst system[35,36,41,45,46] favor the decomposition of Pd_2Ga with a possible subsequent *in situ* formation of PdC_x sites as the true active phase.

4. CONCLUSIONS

Supported nanoparticles of the intermetallic compound Pd_2Ga with a monomodal and narrow particle size distribution can be prepared by decomposition of hydrotalcite-like Pd−Mg−Ga precursors in reducing atmosphere at 773 K. The size of the nanoparticles (2−6 nm) and the amount of Pd^{2+} initially incorporated in the hydrotalcite lattice can be controlled by varying the Pd loading. Pd^{2+} incorporation was evidenced by a combined XANES and TPR study and a critical limit to avoid segregation was found to be ∼1 mol % Pd.

The resulting nano-Pd_2Ga/MgO/$MgGa_2O_4$ materials exhibit a large specific surface area (100−120 m^2 g^{-1}), rendering them to be promising catalytic materials for model studies of the true active state of IMC surfaces. IR spectroscopy of chemisorbed CO revealed different adsorptive properties of the nano-Pd_2Ga particles compared to nano-Pd^0 formed from the same precursor by reduction at lower temperature. Accordingly, the catalytic properties in semihydrogenation of acetylene were found to be superior after high reduction temperature and highly selective catalysts have been obtained. A final stable state of the catalysts was only achieved after long activation with time on stream (TOS) or after oxidative pretreatment. These dynamics of the Pd_2Ga nanoparticles are related to an interplay of surface decomposition into Pd-like surface species and Ga_2O_3 in reactive gas atmosphere, which was also observed by IR spectroscopy in CO atmosphere, and strong metal support interaction between Pd_2Ga nanoparticles and the MgO/$MgGa_2O_4$ support. The active state of the final catalyst can be attributed to a Pd_2Ga core−$Pd/PdC_x/Ga_2O_3$ shell configuration that is difficult to characterize.

This study has shown that the Pd-based intermetallic hydrogenation catalysts can be prepared in a feasible and controlled manner in a nanostructured form. In these catalysts, the known catalytic properties of the bulk intermetallic phases have only apparently been conserved. Instead, a great complexity has been observed, which is related to surface dynamics in reactive atmospheres.

■ ASSOCIATED CONTENT

Supporting Information

Supporting Information includes further discussions and additional experimental details as well as a precipitation protocol (Figure S1), XANES spectra of reference PdZnAl HT sample (Figure S2), XRD patterns of the HTlc precursors (Figure S3) and their evaluation (Table S1), SEM micrographs and EDX line scans of the HTlc precursors (Figure S4) and additional micrographs in the BSE mode of Pd10 and Pd25 (Figure S5), MS data of the TPR experiments (Figure S6), XRD powder pattern of the catalysts after reduction (Figure S7), HRTEM images of selected Pd2Ga particles (Figure S8), IR spectra of CO adsorbed on Pd10 in OH stretching region (Figure S9), additional IR spectra of adsorbed CO (Figure S10), CO chemisorption results (Figure S11), Conversion and selectivity at 473 K over Pd25 (Figure S12), an Arrhenius plot to determine the apparent activation energy (Figure S13), Raman spectra of Pd2Ga25 before and after reaction (Figure S14) and TPO of Pd25 after 44 h time on stream (Figure S15). This material is available free of charge via the Internet at http://pubs.acs.org.

■ AUTHOR INFORMATION

Corresponding Author

*Tel.: +49 30 8413-4408. Fax: +49 30 8413-4405. E-mail: behrens@fhi-berlin.mpg.de.

Notes

The authors declare no competing financial interest.

■ ACKNOWLEDGMENTS

The authors thank Edith Kitzelmann (XRD, Fritz Haber Institute (FHI)), Gudrun Auffermann and Matthias Friedrich (ICP-OES, Max-Planck-Institut für Chemische Physik fester Stoffe (MPI CPfS)), Dirk Rosenthal (Chemisorption, FHI), Gisela Lorenz (BET, FHI), and Marc Willinger (TEM, FHI) for their help with various characterizations. Gregor Wowsnick (FHI) is acknowledged for providing bulk Pd_2Ga as reference sample. The Paul Scherrer Institute (SLS, SuperXAS) is acknowledged for the allocation of beamtime and Olga Safonova and Maarten Nachtegaal for the help with the XANES measurements. Ye Lu (EMPA), Andrey Tarasov and Patrick Kast are acknowledged for their assistance during beamtime. Marc Willinger and Gregor Wowsnick (all FHI) are acknowledged for fruitful discussions.

REFERENCES

(1) Borodziński, A.; Bond, G. C. *Catal. Rev. Sci. Eng.* **2006**, *48*, 91−144.
(2) Bond, G. C.; Dowden, D. A.; Mackenzie, N. *Trans. Faraday Soc.* **1958**, *54*, 1537−1546.
(3) Bond, G. C.; Wells, P. B. In *Advances in Catalysis*, Vol. *15*; Eley, D. D., Pines, H., Weisz, P. B., Eds.; Academic Press: New York, 1965; pp 91−226.
(4) Mallat, T.; Baiker, A. *Appl. Catal., A* **2000**, *200*, 3−22.
(5) Lopez, N.; Vargas-Fuentes, C. *Chem. Commun.* **2012**, *48*, 1379−1391.
(6) Pachulski, A.; Schödel, R.; Claus, P. *Appl. Catal., A* **2012**, *445*−*446*, 107−120.
(7) Studt, F.; Abild-Pedersen, F.; Bligaard, T.; Sørensen, R. Z.; Christensen, C. H.; Nørskov, J. K. *Science* **2008**, *320*, 1320−1322.
(8) Sheth, P. A.; Neurock, M.; Smith, C. M. *J. Phys. Chem. B* **2005**, *109*, 12449−12466.
(9) Huang, D. C.; Chang, K. H.; Pong, W. F.; Tseng, P. K.; Hung, K. J.; Huang, W. F. *Catal. Lett.* **1998**, *53*, 155−159.
(10) Zafeiratos, S.; Piccinin, S.; Teschner, D. *Catal. Sci. Technol.* **2012**, *2*, 1787−1801.
(11) Ota, A.; Armbrüster, M.; Behrens, M.; Rosenthal, D.; Friedrich, M.; Kasatkin, I.; Girgsdies, F.; Zhang, W.; Wagner, R.; Schlögl, R. *J. Phys. Chem. C* **2010**, *115*, 1368−1374.
(12) Osswald, J.; Kovnir, K.; Armbrüster, M.; Giedigkeit, R.; Jentoft, R. E.; Wild, U.; Grin, Y.; Schlögl, R. *J. Catal.* **2008**, *258*, 219−227.
(13) Kovnir, K.; Osswald, J.; Armbrüster, M.; Giedigkeit, R.; Ressler, T.; Grin, Y.; Schlögl, R. In *Studies in Surface Science and Catalysis*, Vol. *162*; Gaigneaux, E. M., Devillers, M., Hermans, S., Jacobs, P. A., Martens, J. A., Ruiz, P., Eds.; Elsevier: Amsterdam, 2006; pp 481−488.
(14) Armbrüster, M.; Kovnir, K.; Behrens, M.; Teschner, D.; Grin, Y.; Schlögl, R. *J. Am. Chem. Soc.* **2010**, *132*, 14745−14747.
(15) Armbrüster, M.; Wowsnick, G.; Friedrich, M.; Heggen, M.; Cardoso-Gil, R. *J. Am. Chem. Soc.* **2011**, *133*, 9112−9118.
(16) He, Y.; Liang, L.; Liu, Y.; Feng, J.; Ma, C.; Li, D. *J. Catal.* **2014**, *309*, 166−173.
(17) Collins, S. E.; Baltanás, M. A.; Garcia Fierro, J. L.; Bonivardi, A. L. *J. Catal.* **2002**, *211*, 252−264.
(18) Penner, S.; Lorenz, H.; Jochum, W.; Stöger-Pollach, M.; Wang, D.; Rameshan, C.; Klötzer, B. *Appl. Catal., A* **2009**, *358*, 193−202.
(19) De Roy, A. *Mol. Cryst. Liq. Cryst. Sci. Technol., Sect. A* **1998**, *311*, 173−193.
(20) Takehira, K.; Shishido, T. *Catal. Surv.y Asia* **2007**, *11*, 1−30.
(21) Rives, V.; Kannan, S. *J. Mater. Chem.* **2000**, *10*, 489−495.
(22) Gérardin, C.; Kostadinova, D.; Coq, B.; Tichit, D. *Chem. Mater.* **2008**, *20*, 2086−2094.
(23) Duan, X.; Evans, D. G. *Layered Double Hydroxides*; Springer−Verlag: Berlin, Heidelberg, 2006.
(24) Forano, C.; Hibino, T.; Leroux, F.; Taviot-Gueho, C. In *Handbook of Clay Science*; Bergaya, F., Theng, B. K. G., Lagaly, G., Eds.; Elsevier: Amsterdam, 2006; p 1021−1095.
(25) Behrens, M.; Kasatkin, I.; Kühl, S.; Weinberg, G. *Chem. Mater.* **2010**, *22*, 386−397.
(26) Shannon, R. *Acta Crystallogr., Sect. A: Cryst. Phys., Diffr., Gen. Crystallogr.* **1976**, *32*, 751−767.
(27) Ota, A.; Kunkes, E. L.; Kasatkin, I.; Groppo, E.; Ferri, D.; Poceiro, B.; Yerga, R. M. N.; Behrens, M. *J. Catal.* **2012**, *293*, 27−38.
(28) Das, N. N.; Srivastava, S. C. *Bull. Mater. Sci.* **2002**, *25*, 283−289.
(29) Eyssler, A.; Mandaliev, P.; Winkler, A.; Hug, P.; Safonova, O.; Figi, R.; Weidenkaff, A.; Ferri, D. *J. Phys. Chem. C* **2010**, *114*, 4584−4594.
(30) Iwasa, N.; Takezawa, N. *Top Catal.* **2003**, *22*, 215−224.
(31) Wannek, C.; Harbrecht, B. *J. Alloys Compd.* **2001**, *316*, 99−106.
(32) Tauster, S. J.; Fung, S. C.; Garten, R. L. *J. Am. Chem. Soc.* **1978**, *100*, 170−175.
(33) Tauster, S. J. *Acc. Chem. Res.* **1987**, *20*, 389−394.
(34) xChe, M.; Bennet, C. O. In *Advances in Catalysis*, Vol. *36*; Eley, D. D., Pines, H., Weisz, P. B., Eds.; Academic Press: New York, 1989; p 55.
(35) Leary, R.; de la Peña, F.; Barnard, J. S.; Luo, Y.; Armbrüster, M.; Meurig Thomas, J.; Midgley, P. A. *ChemCatChem* **2013**, *5*, 2599−2609.
(36) Wowsnick, G.; Teschner, D.; Kasatkin, I.; Girgsdies, F.; Armbrüster, M.; Zhang, A.; Grin, Y.; Schlögl, R.; Behrens, M. *J. Catal.* **2014**, *309*, 209−220.
(37) Sheppard, N.; De La Cruz, C. *Catal. Today* **2001**, *70*, 3−13.
(38) Lear, T.; Marshall, R.; Antonio Lopez-Sanchez, J.; Jackson, S. D.; Klapötke, T. M.; Bäumer, M.; Rupprechter, G.; Freund, H.-J.; Lennon, D. *J. Chem. Phys.* **2005**, *123*, -.
(39) Bertarione, S.; Scarano, D.; Zecchina, A.; Johanek, V.; Hoffmann, J.; Schauermann, S.; Libuda, J.; Rupprechter, G.; Freund, H. J. *J. Catal.* **2004**, *223*, 64−73.
(40) Prinetto, F.; Manzoli, M.; Ghiotti, G.; Martinez Ortiz, M. d. J.; Tichit, D.; Coq, B. *J. Catal.* **2004**, *222*, 238−249.
(41) Föttinger, K. *Catal. Today* **2013**, *208*, 106−112.
(42) Hao, Y.; Mihaylov, M.; Ivanova, E.; Hadjiivanov, K.; Knözinger, H.; Gates, B. C. *J. Catal.* **2009**, *261*, 137−149.
(43) Borchert, H.; Jürgens, B.; Zielasek, V.; Rupprechter, G.; Giorgio, S.; Henry, C. R.; Bäumer, M. *J. Catal.* **2007**, *247*, 145−154.
(44) Föttinger, K.; Schlögl, R.; Rupprechter, G. A. N. *Chem. Commun.* **2008**, 320−322.
(45) Haghofer, A.; Föttinger, K.; Girgsdies, F.; Teschner, D.; Knop-Gericke, A.; Schlögl, R.; Rupprechter, G. *J. Catal.* **2012**, *286*, 13−21.
(46) Wowsnick, G.; Teschner, D.; Armbrüster, M.; Kasatkin, I.; Girgsdies, F.; Grin, Y.; Schlögl, R.; Behrens, M. *J. Catal.* **2014**, *309*, 221−230.
(47) Molero, H.; Bartlett, B. F.; Tysoe, W. T. *J. Catal.* **1999**, *181*, 49−56.
(48) Teschner, D.; Vass, E.; Hävecker, M.; Zafeiratos, S.; Schnörch, P.; Sauer, H.; Knop-Gericke, A.; Schlögl, R.; Chamam, M.; Wootsch, A.; Canning, A. S.; Gamman, J. J.; Jackson, S. D.; McGregor, J.; Gladden, L. F. *J. Catal.* **2006**, *242*, 26−37.
(49) Teschner, D.; Borsodi, J.; Wootsch, A.; Révay, Z.; Hävecker, M.; Knop-Gericke, A.; Jackson, S. D.; Schlögl, R. *Science* **2008**, *320*, 86−89.
(50) Ziemecki, S. B.; Jones, G. A.; Swartzfager, D. G.; Harlow, R. L.; Faber, J. *J. Am. Chem. Soc.* **1985**, *107*, 4547−4548.
(51) Borodziński, A.; Bond, G. C. *Catal. Rev. Sci. Eng.* **2008**, *50*, 379−469.
(52) Osswald, J.; Giedigkeit, R.; Jentoft, R. E.; Armbrüster, M.; Girgsdies, F.; Kovnir, K.; Ressler, T.; Grin, Y.; Schlögl, R. *J. Catal.* **2008**, *258*, 210−218.
(53) Kovnir, K.; Armbruster, M.; Teschner, D.; Venkov, T. V.; Szentmiklosi, L.; Jentoft, F. C.; Knop-Gericke, A.; Grin, Y.; Schlögl, R. *Surf. Sci.* **2009**, *603*, 1784−1792.
(54) Teschner, D.; Revay, Z.; Borsodi, J.; Havecker, M.; Knop-Gericke, A.; Schlögl, R.; Milroy, D.; Jackson, S. D.; Torres, D.; Sautet, P. *Angew. Chem., Int. Ed.* **2008**, *47*, 9274−9278.